Journal of Power Sources 341 (2017) 396–403

Contents lists available at ScienceDirect

Journal of Power Sources

journal homepage: www.elsevier.com/locate/jpowsour

High efficiency $CH_3NH_3PbI_3$:CdS perovskite solar cells with $CuInS_2$ as the hole transporting layer

Chong Chen [a, b, *], Yong Zhai [a, b], Fumin Li [a, b], Furui Tan [a, b], Gentian Yue [a, b], Weifeng Zhang [a, b], Mingtai Wang [c, **]

[a] Henan Key Laboratory of Photovoltaic Materials, Henan University, Kaifeng, 475004, PR China
[b] School of Physics and Electronics, Henan University, Kaifeng, 475004, PR China
[c] Institute of Applied Technology, Hefei Institutes of Physical Science, Chinese Academy of Sciences, Hefei, 230031, PR China

HIGHLIGHTS

- A precursor blending solution method is used to prepare $CH_3NH_3PbI_3$:CdS layer.
- The $CH_3NH_3PbI_3$:CdS bulk heterojunction perovskite solar cells are fabricated.
- The efficiency of the cell is improved due to the introduction of CdS.
- The highest efficiency of prepared $CH_3NH_3PbI_3$:CdS solar cells is (16.5 ± 0.2)%.

GRAPHICAL ABSTRACT

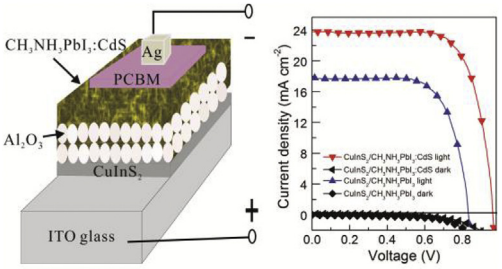

ARTICLE INFO

Article history:
Received 28 September 2016
Received in revised form
2 December 2016
Accepted 6 December 2016

Keywords:
Perovskite
Heterojunction
Solar cells
Efficiency

ABSTRACT

The $CH_3NH_3PbI_3$:CdS composite films are prepared by a newly developed precursor blending solution method, which are further used to fabricate $CH_3NH_3PbI_3$:CdS perovskite solar cells. Our experimental results demonstrate that the introduced CdS effectively improves the light absorption property of the ITO/$CuInS_2$/Al_2O_3/$CH_3NH_3PbI_3$:CdS film stack and decreases the charge recombination in the prepared solar cells due to the formation of $CH_3NH_3PbI_3$/CdS bulk heterojunction. Furthermore, the formed CdS/$CuInS_2$ heterojunction also contributes to the enhanced efficiency. As a consequence, the $CH_3NH_3PbI_3$/CdS bulk heterojunction perovskite solar cells exhibit a maximum power conversion efficiency of (16.5 ± 0.2)%, which is 1.35 times the best efficiency of 12.2% of previously reported CdS/$CH_3NH_3PbI_3$ bilayer solar cell. In addition, this efficiency is a 59% improvement compared with the efficiency of (10.4 ± 0.2)% for the ITO/$CuInS_2$/Al_2O_3/$CH_3NH_3PbI_3$/$PC_{60}BM$/Ag cell without CdS.

1. Introduction

Semiconducting perovskite materials $CH_3NH_3PbX_3$ (X = Cl, Br, I) have recently attracted much attention for photovoltaic applications since the perovskite solar cell with a power conversion efficiency (PCE) of 3.8% was reported in 2009 [1]. Recently, the PCE of perovskite solar cell has increased to more than 20% [2,3]. One of main reasons for the high efficiencies of reported perovskite solar

* Corresponding author. Henan Key Laboratory of Photovoltaic Materials, Henan University, Kaifeng, 475004, PR China.
** Corresponding author.
E-mail addresses: chongchen@henu.edu.cn (C. Chen), mtwang@ipp.ac.cn (M. Wang).

http://dx.doi.org/10.1016/j.jpowsour.2016.12.027
0378-7753/

cells is that perovskite materials have superior electrical and light-harvesting properties, such as a suitable and direct optical band gap, a long hole/electron diffusion length (a few μm), and a high absorption coefficient [4–7]. So far, most of reported perovskite solar cells have a n-i-p planar architecture in the form of n-electron conductor/perovskite/p-hole conductor, in which the perovskite layer acts as both light absorber and carrier transporter [8]. While the planar heterojunction perovskite cells are easily solution-processed, the formation of high quality perovskite layers on electron or hole transporting layer (ETL or HTL) is still a challenging issue. It has been realized that the quality of a perovskite film characterized by its coverage ratio over ETL or HTL layer, purity and morphology, as well as the crystal particle size, has important effects on the performance of the perovskite solar cells. A high quality perovskite layer should be continuous, uniform, and compact over the substrate surface. For this requirement, two typical strategies, i.e., vapor deposition and solution process, are developed. Snaith' group and Bolink' group have fabricated planar heterojunction cells with a PCE of over 12% under AM 1.5G irradiation (100 mW cm^{-2}) by the formation of compact and continuous perovskite layer [8]. However, the vapor deposition process normally requires a high vacuum, which will not facilitate the large scale fabrication. In contrast, the solution process has the advantages of low manufacturing cost and mass production, which typically includes one-step and two-step solution methods [9]. The one-step solution method involves a simple one-step spin coating process of perovskite precursor solution. The two-step method involves spin coating PbI_2 film and the sequential formation of crystalline perovskite film at a thermal annealing process. However, these solution methods are suffering from the difficulty in achieving the compact and homogenous perovskite film for planar perovskite solar cells. Typically, the perovskite film prepared by the two-step solution method is usually not well crystallized and easily detached from the underlying substrate [10], while that prepared by the one-step solution method is often non-continuous with a lot of pinholes. One main reason for the low compactness of pure perovskite film is the formation of perovskite crystal particles during the perovskite crystallization process. These individual crystal particles are scattered and the connection between the particles are loose.

To overcome the morphology problem, several various kinds of additives, such as 1, 8-diiodooctane (DIO), 1-chloronaphthalene, and N-cyclohexyl-2-pyrrolidone are added to perovskite precursor to modify the crystallization process [11–13]. In addition, solvent engineering method is also developed to fabricate uniform and compact perovskite film [14]. Although the quality of perovskite film prepared by these methods has been improved, these methods do not have very strong operability due to the complexity of the film fabrication process.

In this study, we demonstrate an in-situ nanoparticle-blending strategy to prepare high quality $CH_3NH_3PbI_3$:CdS photoactive layer for the ITO/$CuInS_2$/Al_2O_3/$CH_3NH_3PbI_3$:CdS/$PC_{60}BM$/Ag perovskite solar cells based on $CH_3NH_3PbI_3$:CdS bulk heterojunctions for the first time. Recently, CdS has been coated onto the surface of TiO_2 layer to enhance stability of perovskite solar cells [15,16]. However, the perovskite solar cell based on $CH_3NH_3PbI_3$:CdS bulk heterojunction has not been reported so far.

Fig. 1 shows the architecture and energy level alignments of the fabricated solar cells. The in-situ formation of CdS nanocrystals in $CH_3NH_3PbI_3$ matrix results in a three-dimensionally interconnected $CH_3NH_3PbI_3$:CdS composite layer in the porous Al_2O_3 scaffold for light absorption. The $CuInS_2$ and $PC_{60}BM$ layers act as the HTL and ETL, respectively. Our results demonstrate that the introduced CdS improves the quality of perovskite layer. More importantly, the CdS leads to a more effective charge transfer at the

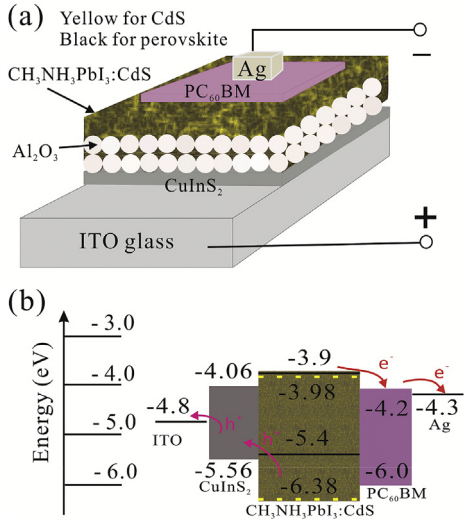

Fig. 1. (a) Schematic diagram and (b) energy diagram of the ITO/$CuInS_2$/Al_2O_3/$CH_3NH_3PbI_3$:CdS/$PC_{60}BM$/Ag solar cells.

HTL/$CH_3NH_3PbI_3$:CdS, $CH_3NH_3PbI_3$/CdS, and $CH_3NH_3PbI_3$:CdS/ETL interfaces mainly due to the lower conduction band (CB) level of CdS than that of the $CH_3NH_3PbI_3$ [17], and thus reduces the charge recombination in the cells. Moreover, the formed CdS/$CuInS_2$ heterojunction could contribute to the photocurrent, which may be one of the reasons for the outstanding current of fabricated $CH_3NH_3PbI_3$/CdS bulk heterojunction perovskite cells. The obtained highest efficiency of (16.5 ± 0.2)% is much higher than that (12.2%) of previously reported CdS/$CH_3NH_3PbI_3$ bilayer solar cell [16]. Our results show that the $CH_3NH_3PbI_3$:CdS blend material is much more efficient than pristine $CH_3NH_3PbI_3$ for the improvement of device performance.

2. Experimental section

2.1. ITO/$CuInS_2$/Al_2O_3 synthesis

To prepare the ITO/$CuInS_2$ film stack, we synthesized $CuInS_2$ nanocrystals on cleaned ITO substrate by the procedure described elsewhere [18]. The $CuInS_2$ precursor solution was prepared by dissolving 0.11 mmol of CuI, 0.1 mmol of $In(OAc)_3$, and 0.5 mmol of thiourea in a mixture of 1-butylamine (0.6 mL) and 1-propionic acid (40 μL) under an nitrogen atmosphere in a glovebox (O_2 < 0.1 ppm, H_2O < 0.1 ppm). After that, the obtained $CuInS_2$ precursor solution was spin-cast onto the cleaned ITO substrates at 2000 rpm for 30 s. The substrates were heat-treated at 150 °C for 10 min and 250 °C for 15 min. The characterizations of ITO/$CuInS_2$ film stack are provided in Fig. S1, where a condensed $CuInS_2$ film of 130 nm in thickness consisting of the tetragonal $CuInS_2$ nanoparticles of 20–30 nm in size is deposited on ITO substrate. In order to obtain ITO/$CuInS_2$/Al_2O_3 film stack, the isopropanol solution containing Al_2O_3 nanoparticles was spin-cast (3000 rpm, 60 s) onto the prepared ITO/$CuInS_2$ film stack, followed by the thermal annealing at 150 °C for 15 min. The characterizations of ITO/$CuInS_2$/Al_2O_3 film stack are provided in Fig. S2.

2.2. Device fabrication

First, to prepare the precursor solution of $CH_3NH_3PbI_3$:CdS blend, the synthesized CH_3NH_3I was first dissolved with PbI_2 at a 1:1mol ratio in 2 mL N, N-dimethylformamide (DMF) (40% by weight) at 60 °C with vigorous stirring for 12 h to obtain pure

$CH_3NH_3PbI_3$ precursor solution. After that, $CdCl_2$ (0.2 mmol) and thiourea (0.6 mmol) were dissolved in the obtained $CH_3NH_3PbI_3$ precursor solution with stirring for 30 min to obtain $CH_3NH_3PbI_3$:CdS precursor solution. Then, the prepared ITO/$CuInS_2$/Al_2O_3 film stacks were spin-coated with the obtained $CH_3NH_3PbI_3$/CdS precursor solution at 3000 rpm for 60 s, after which the film stacks are dried at 100 °C for 30 min to form crystalline CdS and $CH_3NH_3PbI_3$. CdS is obtained by the chemical reaction of thiourea with $CdCl_2$. Then the 1,2-dichlorobenzene (DCB) solution that contains [6,6]-phenyl-C61-butyric acid methyl esther ($PC_{60}BM$) (20 mg/mL) was spin cast onto the prepared ITO/$CuInS_2$/Al_2O_3/$CH_3NH_3PbI_3$:CdS film stack at 1000 rpm for 60 s, after which the film stack was annealed at 100 °C for 5 min. All the experiment was finished in a nitrogen glovebox ($O_2 < 0.1$ ppm, $H_2O < 0.1$ ppm). Finally, the silver electrodes were thermally evaporated at low pressure ($<1 \times 10^{-6}$ Torr) from a silver wire (99.999%) to complete the fabrication of ITO/$CuInS_2$/Al_2O_3/$CH_3NH_3PbI_3$:CdS/$PC_{60}BM$/Ag device. For comparison, the ITO/$CuInS_2$/Al_2O_3/$CH_3NH_3PbI_3$/$PC_{60}BM$/Ag cells without CdS are also fabricated by the similar fabrication process described above. The only difference is that the $CH_3NH_3PbI_3$ film is fabricated from the pure $CH_3NH_3PbI_3$ precursor solution. In addition, To explain the obtained high photocurrent densities of the ITO/$CuInS_2$/Al_2O_3/$CH_3NH_3PbI_3$:CdS/$PC_{60}BM$/Ag cells, the ITO/$CuInS_2$/CdS/Ag cells are fabricated. A detailed fabrication process of ITO/$CuInS_2$/CdS/Ag cell can be obtained from previous publication [18].

2.3. Characterization

Scanning electron microscopy (SEM) measurements were performed on a field-emission scanning electron microscope (FESEM, JSM-7001F). Transmission electron microscopy (TEM) and high-resolution TEM (HRTEM) studies were done on a JEOL-2010 microscope under an acceleration voltage of 200 kV. The pure $CH_3NH_3PbI_3$ and $CH_3NH_3PbI_3$:CdS blend samples for TEM and XRD observations were deposited on clean glass substrates to exclude the influence of other materials (i.e., $CuInS_2$ and Al_2O_3) on measurement. A portion of $CH_3NH_3PbI_3$:CdS sample was scratched from the glass substrate in1,2-dichlorobenzene (DCB) solution, followed by ultrasonication for a few minutes. Then a drop of DCB was placed on a copper grid and subjected to TEM and HRTEM measurements. The crystalline phase and structure were studied by X-ray diffractometer (XRD, DX-2500; Dandong Fangyuan Instrument Co., Ltd., Dandong, China). The atomic force microscopy (AFM) measurements were performed using an Agilent 5500 AFM (Agilent Technologies, AZ, USA). The absorption spectra were obtained by a Shimadzu UV-2550 spectrophotometer.

The photoluminescence (PL) spectra of the films were recorded by using the HORIBA Jobin Yvon Fluorolog-3 Spectrofluorometer system with Xe 900 (450 W xenon arc lamp) as the light source. Time-resolved fluorescence analyses were performed on an Edinburgh Instrument FLS 980 photoluminescence spectrometer. All measurements were performed at room temperature in ambient atmosphere (30% relative humidity). The used light source is a 515 nm pulsed diode laser (EPL-515, typical average power@20 Mhz: 0.1 mW, maximum pulse width@10 Mhz: 320 ps). Reconvolution fit analysis was used to fit a measured sample decay to a model function with three exponential terms. The quality of the fit was estimated by the parameter χ^2 ($0.90 \leq \chi^2 \leq 1.10$) and the symmetrical distribution of the residuals about the zero axis.

All *J-V* measurements are performed using a Keithley 2410 source meter (Cleveland, OH, USA) under air atmosphere, and the as-prepared devices were illuminated with an AM 1.5 G solar simulator (Newport Inc., Irvine, CA, USA). The irradiation intensity is calibrated by a Si reference diode (100 mW cm^{-2}). During the *J-V* measurements, the ITO and Ag contacts were taken as positive and negative electrodes, respectively. *J-V* characteristics of prepared solar cells are measured in forward (from 1.0 V to 0 V) and reverse (from 0 V to 1.0 V) modes. For all measurements, the effective illumination area of the cells was 4 mm^2, which was determined by an opaque mask to avoid the diffuse light penetrating into the active layer in the cells. The incident monochromatic photon-to current conversion efficiency (IPCE) curves were measured with a solar cell QE/IPCE measurement system (Solar Cell Scan 100, Beijing Zolix Instruments Co. Ltd., China). The electrochemical impedance spectroscopy (EIS) of the fabricated cells was performed using a CHI660E (Chenhua Device Company, Shanghai, China) electrochemical measurement system at 20 °C in ambient atmosphere under illumination (100 mW/cm^2) with an applied potential (0.7 V). The frequencies scanned were in the 1 MHz–100 mHz range. The resultant impedance spectra were simulated using the Z-view software.

3. Results and discussions

Fig. 2a and b show the typically top-view SEM images of as-prepared ITO/$CuInS_2$/Al_2O_3/$CH_3NH_3PbI_3$ and ITO/$CuInS_2$/Al_2O_3/$CH_3NH_3PbI_3$:CdS film stacks at 1000× magnification, respectively. It can be seen that, compared with the ITO/$CuInS_2$/Al_2O_3/$CH_3NH_3PbI_3$ film stack without CdS, the flatness and compactness of the ITO/$CuInS_2$/Al_2O_3/$CH_3NH_3PbI_3$:CdS film stack have been improved significantly after the introduction of CdS. To observe the surface morphology of the film stacks more clearly, Fig. 2c and d show the top-view SEM images of the ITO/$CuInS_2$/Al_2O_3/$CH_3NH_3PbI_3$ and ITO/$CuInS_2$/Al_2O_3/$CH_3NH_3PbI_3$:CdS film stacks at 20,000× magnification, respectively. By comparing Fig. 2c and d, it can be seen that the size of the voids in the ITO/$CuInS_2$/Al_2O_3/$CH_3NH_3PbI_3$:CdS film stack becomes smaller and the number of the voids has also be reduced, which indicates that the ITO/$CuInS_2$/Al_2O_3/$CH_3NH_3PbI_3$:CdS film stack has better compactness than the ITO/$CuInS_2$/Al_2O_3/$CH_3NH_3PbI_3$ film stack. Fig. 2e shows the cross-sectional SEM image of the ITO/$CuInS_2$/Al_2O_3/$CH_3NH_3PbI_3$:CdS film stack, which shows that the film stack has an average thickness of about 800 nm. It can be seen that the $CH_3NH_3PbI_3$:CdS blend penetrated into the pores inside Al_2O_3 layer and reached the $CuInS_2$ layer, resulting in the formation of the $CH_3NH_3PbI_3$/$CuInS_2$ and CdS/$CuInS_2$ heterojuctions. The AFM results (Fig. S3) further show that the $CH_3NH_3PbI_3$:CdS film over Al_2O_3 layer has a quite smooth surface with a root-mean-square (RMS) roughness of 3.4 nm measured at an area of 2×2 μm^2. These SEM and AFM images demonstrate that the $CH_3NH_3PbI_3$:CdS blend formed a continuous, uniform, and compact film over the ITO/$CuInS_2$/Al_2O_3 substrate.

To demonstrate the formation of both $CH_3NH_3PbI_3$ and CdS, the crystallinity of the $CH_3NH_3PbI_3$:CdS composite film on the pure glass substrate was characterized by XRD (see Fig. S4). The structure of the $CH_3NH_3PbI_3$ is well consistent with the previous report [19]. The $CH_3NH_3PbI_3$:CdS blend film exhibits both the XRD patterns of $CH_3NH_3PbI_3$ and CdS components, where the diffraction peaks at 28.53° and 43.87° are indexed to the (214) and (107) lattice planes of orthorhombic CdS (PDF# 47-1179), respectively. Clearly, the $CH_3NH_3PbI_3$:CdS composite film prepared by our method actually consists of $CH_3NH_3PbI_3$ and CdS crystals.

Fig. 3a shows a typical TEM image of the $CH_3NH_3PbI_3$ nanoparticles with the surface decorated with CdS. The small spherical CdS nanoparticles are observed on the $CH_3NH_3PbI_3$ surface, which clearly demonstrates the coexistence of $CH_3NH_3PbI_3$ and CdS crystals. The CdS nanocrystals are present in the form of spherical particles with a size in the range from a few to tens of nanometers. The $CH_3NH_3PbI_3$ crystals are in the form of cuboids with clear diamond shaped edges, which is in agreement with previous report

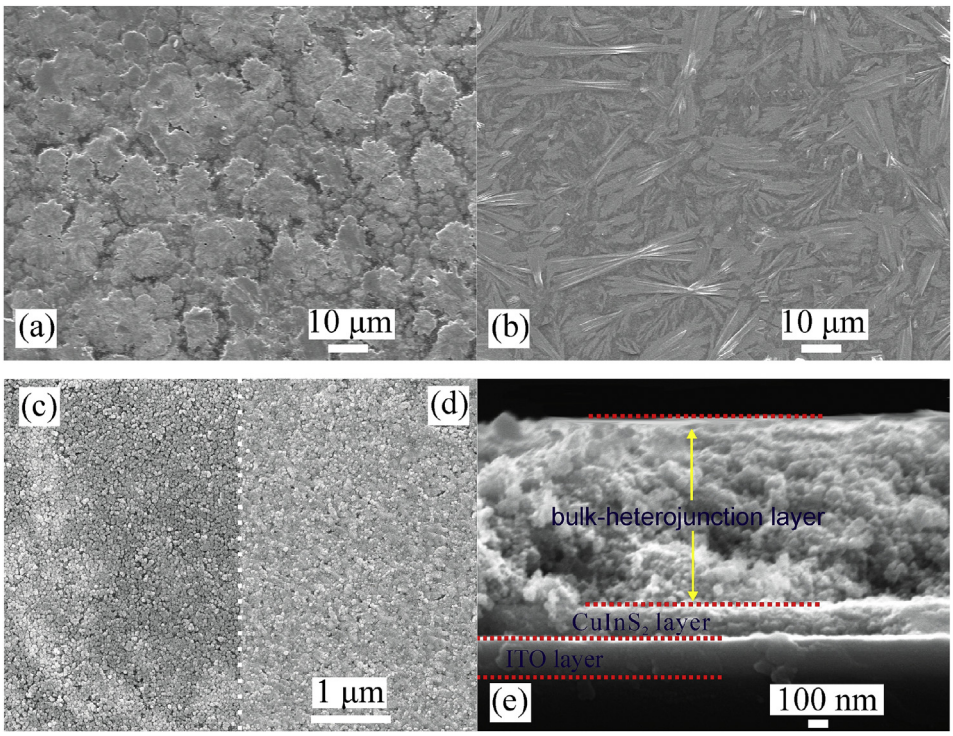

Fig. 2. Top-view SEM images of as-prepared (a) ITO/$CuInS_2$/Al_2O_3/$CH_3NH_3PbI_3$ and (b) ITO/$CuInS_2$/Al_2O_3/$CH_3NH_3PbI_3$:CdS film stacks at 1000× magnification. Top-view SEM images of the (c) ITO/$CuInS_2$/Al_2O_3/$CH_3NH_3PbI_3$ and (d) ITO/$CuInS_2$/Al_2O_3/$CH_3NH_3PbI_3$:CdS film stacks at 20,000× magnification. (e) Cross-sectional SEM image of the ITO/$CuInS_2$/Al_2O_3/$CH_3NH_3PbI_3$:CdS film stack.

[20,21]. The size of $CH_3NH_3PbI_3$ cuboids ranges from tens of nanometers to more than one hundred nanometers (see Fig. S3 c).

Fig. 3b shows the low-magnification TEM image of $CH_3NH_3PbI_3$:CdS composite film. Fig. 3c and d show the HRTEM images of CdS and $CH_3NH_3PbI_3$ crystals, respectively. In the film, it can be seen that the formed CdS nanocrystals can be connected with each other. As shown in Fig. 3c, the spherical crystals exhibit a lattice fringe spacing of 0.357 nm, corresponding to the (400) lattice planes of orthorhombic CdS (PDF# 47-1179), while the observed lattice fringe spacing of 0.317 nm in Fig. 3d can be attributed to the (220) plane of tetragonal phase of the $CH_3NH_3PbI_3$ perovskite [19,22]. Clearly, the $CH_3NH_3PbI_3$:CdS blend layer consist of $CH_3NH_3PbI_3$ and CdS crystals, which agrees with the XRD data (Fig. S4). It can be concluded from the above data that the CdS nanocrystals are formed during the preparation of $CH_3NH_3PbI_3$:CdS photoactive layer in solar cells.

Fig. 4a shows the UV–vis absorption spectra of the ITO/$CuInS_2$, ITO/$CuInS_2$/Al_2O_3/$CH_3NH_3PbI_3$, and ITO/$CuInS_2$/Al_2O_3/$CH_3NH_3PbI_3$:CdS film stacks. For the ITO/$CuInS_2$, an exponential-shaped absorption line is observed, which is very similar to characteristic absorption curve of pure $CuInS_2$ film. Therefore, this result further confirms the formation of $CuInS_2$. After the deposition of $CH_3NH_3PbI_3$, the absorbance of the spectra of the ITO/$CuInS_2$/Al_2O_3/$CH_3NH_3PbI_3$ film stack significantly increased in the wavelength region from 350 to 850 nm compared with the ITO/$CuInS_2$ without the $CH_3NH_3PbI_3$ film. The reason for this should be that the formed $CH_3NH_3PbI_3$ has a strong light absorption in the wavelength from 350 to 850 nm [23]. After the introduction of CdS, a further increase in the absorbance of the spectra of the ITO/$CuInS_2$/Al_2O_3/$CH_3NH_3PbI_3$:CdS film stack is observed compared with the ITO/$CuInS_2$/Al_2O_3/$CH_3NH_3PbI_3$ film stack. Moreover, for the ITO/$CuInS_2$/Al_2O_3/$CH_3NH_3PbI_3$:CdS film stack, it can be found that the absorbance of the spectra increases mainly in the wavelength region from 400 to 750 nm, which is mainly due to the light absorption of CdS [24] and the formation of more compact $CH_3NH_3PbI_3$:CdS film. It should be noted that, compared with the ITO/$CuInS_2$/Al_2O_3/$CH_3NH_3PbI_3$ film stack without CdS, the introduced CdS did not lead to an increase in the thickness of the ITO/$CuInS_2$/Al_2O_3/$CH_3NH_3PbI_3$:CdS film stack (see Fig. 2e and Fig. S2 b), which indicates that the thickness of the ITO/$CuInS_2$/Al_2O_3/$CH_3NH_3PbI_3$:CdS film stack should not be the main reason for the increased light absorption. There reason for this phenomenon may be that the thickness of the ITO/$CuInS_2$/Al_2O_3/$CH_3NH_3PbI_3$:CdS film stack is mainly determined by the thickness of the Al_2O_3 layer (see Fig. S2 b). These results further confirm the formation of $CH_3NH_3PbI_3$ and CdS and indicate that introduced CdS can effectively improve the light absorption property of the ITO/$CuInS_2$/Al_2O_3/$CH_3NH_3PbI_3$:CdS film stack.

To further investigate the effect of formed $CH_3NH_3PbI_3$/CdS interface on the electron–hole dynamics, the PL spectra of the ITO/$CuInS_2$/Al_2O_3/$CH_3NH_3PbI_3$ and ITO/$CuInS_2$/Al_2O_3/$CH_3NH_3PbI_3$:CdS film stacks are measured and the results are shown in Fig. 4b. The upper and lower insets show the PL spectra in the wavelength range of 450–530 nm and the charge transfer at the $CH_3NH_3PbI_3$/CdS interface, respectively. The upper inset shows that the PL emission intensity of the ITO/$CuInS_2$/Al_2O_3/$CH_3NH_3PbI_3$:CdS film stack is obviously higher than that of the ITO/$CuInS_2$/Al_2O_3/$CH_3NH_3PbI_3$ film stack, resulting from PL emission of CdS in the wavelength range of 450–530 nm. However, the ITO/$CuInS_2$/Al_2O_3/$CH_3NH_3PbI_3$:CdS film stack exhibited relatively lower PL emission in the wavelength range of 530–850 nm. As shown in the lower inset of Fig. 4b, more effective charge transfer in the ITO/$CuInS_2$/Al_2O_3/$CH_3NH_3PbI_3$:CdS film stack may occur at the $CH_3NH_3PbI_3$/CdS interface, which leads to the quenched PL emission of the ITO/$CuInS_2$/Al_2O_3/$CH_3NH_3PbI_3$:CdS film stack.

To characterize carrier recombination of pure $CH_3NH_3PbI_3$ and

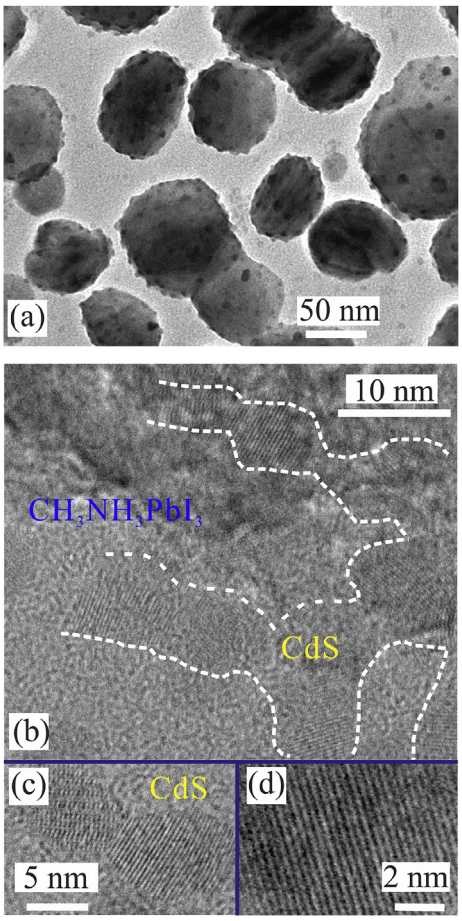

Fig. 3. (a) A typical TEM image of the $CH_3NH_3PbI_3$ nanoparticles with the surface decorated with CdS. (b) Low-magnification TEM image of the $CH_3NH_3PbI_3$:CdS composite film. HR-TEM images of the (c) CdS and (d) $CH_3NH_3PbI_3$ nanaoparticles.

$CH_3NH_3PbI_3$:CdS films prepared on glass substrates, Time-resolved PL decay transients are measured at 775 nm and shown in Fig. 4c. It can be seen that, the carrier lifetime (τ) of $CH_3NH_3PbI_3$:CdS composite film is 184.1 ns, which is much longer than that (41.6 ns) of pure $CH_3NH_3PbI_3$. To explain the time-resolved PL results, the charge transfer processes (1) and (2) for pure $CH_3NH_3PbI_3$ and $CH_3NH_3PbI_3$:CdS films are displayed in the inset of Fig. 4c, respectively. As shown in the charge transfer process (1), for the $CH_3NH_3PbI_3$, the fluorescence generation only involves one-step charge transfer, which is that the excited electrons in pure $CH_3NH_3PbI_3$ jump from the conduction band (CB) to the valance band (VB), leading to the photoluminescence. However, for the $CH_3NH_3PbI_3$:CdS film, the fluorescence generation involves a two-step charge transfer as shown in the charge transfer process (2). The excited electrons in the $CH_3NH_3PbI_3$ can first jump to the CdS, and then recombine with the holes in the $CH_3NH_3PbI_3$ through the $CH_3NH_3PbI_3$/CdS interface, which prolongs the lifetime of the carriers. It is worth noting that the CB level of CdS is very close to that of the $CH_3NH_3PbI_3$, which indicates that the fluorescence wavelength is almost as the same as that of the pure $CH_3NH_3PbI_3$ after the charge recombination between the electrons in the CdS and the holes in the $CH_3NH_3PbI_3$. Therefore, for both pure $CH_3NH_3PbI_3$ and $CH_3NH_3PbI_3$:CdS films, the same PL wavelength (i.e., 775 nm) is chosen to monitor. The time-resolved PL results further confirm the charge transfer from the $CH_3NH_3PbI_3$ to the CdS.

Fig. 5 shows the measured *J*–*V* characteristics of the best performing ITO/$CuInS_2$/CdS/Ag, ITO/$CuInS_2$/Al_2O_3/$CH_3NH_3PbI_3$/$PC_{60}BM$/Ag and ITO/$CuInS_2$/Al_2O_3/$CH_3NH_3PbI_3$:CdS/$PC_{60}BM$/Ag cells under simulated AM 1.5 illumination (100 mW cm^{-2}) and dark

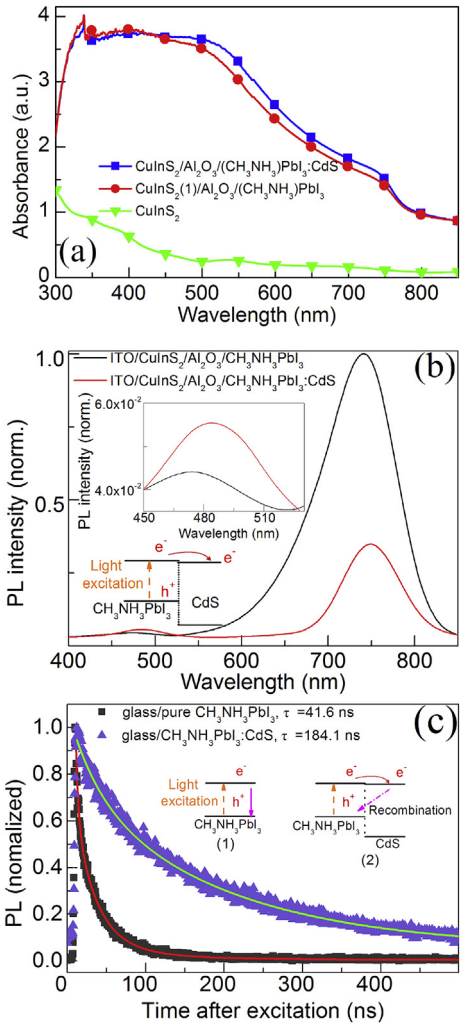

Fig. 4. (a) UV–vis absorption spectra of the ITO/$CuInS_2$, ITO/$CuInS_2$/Al_2O_3/$CH_3NH_3PbI_3$ and ITO/$CuInS_2$/Al_2O_3/$CH_3NH_3PbI_3$:CdS film stacks. (b) Photoluminescence spectra of the ITO/$CuInS_2$/Al_2O_3/$CH_3NH_3PbI_3$ and ITO/$CuInS_2$/Al_2O_3/$CH_3NH_3PbI_3$:CdS film stacks. Excitation at 378 nm. (c) Normalized photoluminescence decay dynamics of pure $CH_3NH_3PbI_3$ and $CH_3NH_3PbI_3$:CdS films probed at 775 nm after excitation at 515 nm. The solid lines are fitted results with a polynomial exponential decay. The fitting of measured data leads to a lifetime (τ) of free carriers after photoexcitation. Charge transfer process (1) for pure $CH_3NH_3PbI_3$ and Charge transfer process (2) for $CH_3NH_3PbI_3$:CdS film.

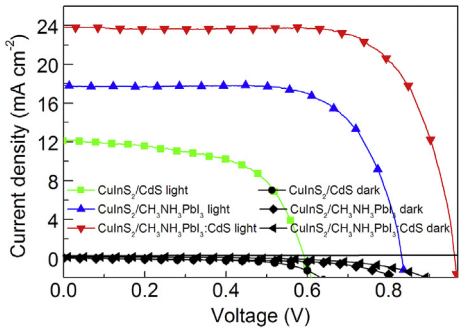

Fig. 5. *J*–*V* characteristics of the ITO/$CuInS_2$/CdS/Ag, ITO/$CuInS_2$/Al_2O_3/$CH_3NH_3PbI_3$/$PC_{60}BM$/Ag and ITO/$CuInS_2$/Al_2O_3/$CH_3NH_3PbI_3$:CdS/$PC_{60}BM$/Ag cells.

conditions. The corresponding four solar cell parameters: open-circuit voltage (V_{oc}), short-circuit photocurrent (J_{sc}), fill factor (FF), and PCE, are reported in Table 1.

It can be found that, compared with the ITO/$CuInS_2$/Al_2O_3/$CH_3NH_3PbI_3$/$PC_{60}BM$/Ag cell without CdS in the active layer, an increase in all parameters is observed from Table 1 for the ITO/$CuInS_2$/Al_2O_3/$CH_3NH_3PbI_3$:CdS/$PC_{60}BM$/Ag cell. The increase in V_{oc} and FF is obvious. Moreover, the J_{sc} of the ITO/$CuInS_2$/Al_2O_3/$CH_3NH_3PbI_3$:CdS/$PC_{60}BM$/Ag cell also shows a great improvement. It can be seen from Table 1 that the J_{sc} increased to (23.8 ± 0.2) mA cm^{-2}, which is a 33.7% improvement compared with the J_{sc} of (17.8 ± 0.3) mA cm^{-2} for as-prepared ITO/$CuInS_2$/Al_2O_3/$CH_3NH_3PbI_3$/$PC_{60}BM$/Ag cell. In fact, a larger J_{SC} could be reached in our cells. However, the corresponding PCE decreased due to the generally reduced FF, suggesting that there is still room to further increase the performance of the cells. The highest PCE of (16.5 ± 0.2)% was achieved for the ITO/$CuInS_2$/Al_2O_3/$CH_3NH_3PbI_3$:CdS/$PC_{60}BM$/Ag cell, corresponding to an increase of 59% as compared to the ITO/$CuInS_2$/Al_2O_3/$CH_3NH_3PbI_3$/$PC_{60}BM$/Ag cell without CdS. This high PCE is much higher than that 12.2% of reported CdS/$CH_3NH_3PbI_3$ bilayer solar cells [16], confirming the superiority of the bulk-heterojunction structure. Fig. S5 shows the characteristics measured via forward and reverse bias sweep for the ITO/$CuInS_2$/Al_2O_3/$CH_3NH_3PbI_3$:CdS/$PC_{60}BM$/Ag cell. It can be seen that the hysteresis is not obvious. Apparently, the PCE of the ITO/$CuInS_2$/Al_2O_3/$CH_3NH_3PbI_3$:CdS/$PC_{60}BM$/Ag cell has been greatly improved due to the introduction of CdS.

To investigate the effect of introduced CdS on the charge transfer kinetics of the ITO/$CuInS_2$/Al_2O_3/$CH_3NH_3PbI_3$:CdS/$PC_{60}BM$/Ag cell, the electrochemical impedance spectroscopy (EIS) of both ITO/$CuInS_2$/Al_2O_3/$CH_3NH_3PbI_3$:CdS/$PC_{60}BM$/Ag and ITO/$CuInS_2$/Al_2O_3/$CH_3NH_3PbI_3$/$PC_{60}BM$/Ag cells under an illumination intensity of 100 mW cm^{-2} with an applied potential of 0.7 V was measured and the results were shown in Fig. 6. The resulting impedance spectra were fitted using the equivalent circuit shown in Fig. 6. The parameters obtained from the impedance spectra fits for the ITO/$CuInS_2$/Al_2O_3/$CH_3NH_3PbI_3$:CdS/$PC_{60}BM$/Ag and ITO/$CuInS_2$/Al_2O_3/$CH_3NH_3PbI_3$/$PC_{60}BM$/Ag cells are presented in Table 2. The shape of the measured Nyquist plots is similar to previously reported results [25]. To characterize the charge transfer kinetics of the solar cells, the equivalent circuit shown in the inset is used for impedance fits [26,27]. For the solar cells, the R_s is the ohmic series resistance, including the sheet resistance of the $CuInS_2$ layer, the $PC_{60}BM$ layer, and the $CH_3NH_3PbI_3$ (or $CH_3NH_3PbI_3$:CdS) resistance. The first semicircle at high frequency refers to the R_{CT1} for the charge-transfer resistance at the HTL/photoactive layer interface. The second semicircle at middle frequency refers to the R_{CT2} for the charge-transfer resistance at the photoactive layer/ETL interface. The lower charge-transfer resistances (i.e., R_{CT1} and R_{CT2}) could result in a more effective charge-transfer and a rapid transporting ability for the electron and hole, which would lead to a reduced charge recombination in the cells. It can be clearly seen from Table 2 that, compared with the ITO/$CuInS_2$/Al_2O_3/$CH_3NH_3PbI_3$/$PC_{60}BM$/Ag, both R_{CT1} and R_{CT2} of the ITO/$CuInS_2$/Al_2O_3/$CH_3NH_3PbI_3$:CdS/$PC_{60}BM$/Ag cell decreased significantly, which indicates that the charge recombination at the $CuInS_2$/$CH_3NH_3PbI_3$:CdS and the $CH_3NH_3PbI_3$:CdS/$PC_{60}BM$ interfaces could be effectively reduced due to the introduction of CdS and would further improve the performance of the ITO/$CuInS_2$/Al_2O_3/$CH_3NH_3PbI_3$:CdS/$PC_{60}BM$/Ag cell with CdS.

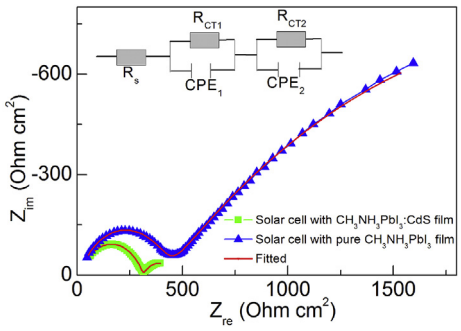

Fig. 6. Nyquist plots of the ITO/$CuInS_2$/Al_2O_3/$CH_3NH_3PbI_3$:CdS/$PC_{60}BM$/Ag and ITO/$CuInS_2$/Al_2O_3/$CH_3NH_3PbI_3$/$PC_{60}BM$/Ag under an illumination intensity of 100 mW cm^{-2} with an applied potential 0.7 V. Frequencies scanned were in the 1 MHz−100 mHz range. The inset is the equivalent circuit used for the impedance fits. EIS measurements are shown in the solid markers, and equivalent circuit fits are represented by the red solid lines. (For interpretation of the references to colour in this figure legend, the reader is referred to the web version of this article.)

To explain the obtained EIS results, possible charge transfer paths in the cell are summarized, as shown in Fig. 7. For the ITO/$CuInS_2$/Al_2O_3/$CH_3NH_3PbI_3$/$PC_{60}BM$/Ag cell without CdS, only charge transfer path 1 exists. The pure $CH_3NH_3PbI_3$ film acts as a transporting layer for both electrons and holes, which may cause the recombination of photogenerated charges in the perovskite photoactive layer. However, for the ITO/$CuInS_2$/Al_2O_3/$CH_3NH_3PbI_3$:CdS/$PC_{60}BM$/Ag cell, not only path 1, but also path 2 and path 3 may also exist. For the charge transfer path 2, due to the formation of $CH_3NH_3PbI_3$/CdS heterojunction in the $CH_3NH_3PbI_3$:CdS composite film, the photogenerated electrons in the $CH_3NH_3PbI_3$ can be first transferred to the CdS through the $CH_3NH_3PbI_3$/CdS interface because of the lower CB level of CdS than that of $CH_3NH_3PbI_3$ (Fig. 1b), [15] which could decrease the probability of charge recombination in the photoactive layer due to the spatial separation of photogenerated electrons and holes. The obtained PL spectra and time-resolved PL results can support this explanation (Fig. 4b and c). Therefore, the formed $CH_3NH_3PbI_3$/CdS bulk heterojunction in the ITO/$CuInS_2$/Al_2O_3/$CH_3NH_3PbI_3$:CdS/$PC_{60}BM$/Ag cell may effectively reduce the charge recombination in the $CH_3NH_3PbI_3$:CdS photoactive layer. The electrons in the CdS are further transferred to the $PC_{60}BM$ layer and the holes in the $CH_3NH_3PbI_3$ are transferred to the $CuInS_2$ through the $CuInS_2$/$CH_3NH_3PbI_3$ interface. For the charge transfer path 3, due to the formation of CdS/$CuInS_2$ heterojunction on the $CuInS_2$ film (Fig. 2e), the photogenerated electrons in the CdS may be directly transferred to the $PC_{60}BM$ layer and the holes are collected by the $CuInS_2$. Therefore, for the ITO/$CuInS_2$/Al_2O_3/$CH_3NH_3PbI_3$:CdS/$PC_{60}BM$/Ag cell, the holes at the $CuInS_2$/$CH_3NH_3PbI_3$:CdS interface can be transferred through both $CuInS_2$/$CH_3NH_3PbI_3$ and $CuInS_2$/CdS interfaces leading a decreased R_{CT1}, and the electrons can be transferred to $PC_{60}BM$ layer through both $CH_3NH_3PbI_3$/$PC_{60}BM$ and CdS/

Table 1
Summary of solar cell performances under simulated AM 1.5G solar irradiation.

Devices	V_{oc} (V)	J_{sc} (mA cm^{-2})	FF	PCE (%)
ITO/$CuInS_2$/Al_2O_3/$CH_3NH_3PbI_3$:CdS/$PC_{60}BM$/Ag	0.950	23.8 ± 0.2	0.73	16.5 ± 0.2
ITO/$CuInS_2$/Al_2O_3/$CH_3NH_3PbI_3$/$PC_{60}BM$/Ag	0.835	17.8 ± 0.3	0.69	10.4 ± 0.2
ITO/$CuInS_2$/CdS/Ag	0.589	12.1 ± 0.3	0.59	4.2 ± 0.2

Table 2
The fitting parameters.

Devices	*Rs* (Ω cm^2)	R_{CT1} (mA cm^{-2})	R_{CT2} (mA m^{-2})	CPE_1 (mF cm^{-2})	CPE_2 (μF cm^{-2})
Solar cells with $CH_3NH_3PbI_3$:CdS	12	187	297	2.640	0.20
Solar cells with pure $CH_3NH_3PbI_3$	11	4580	408	0.266	0.18

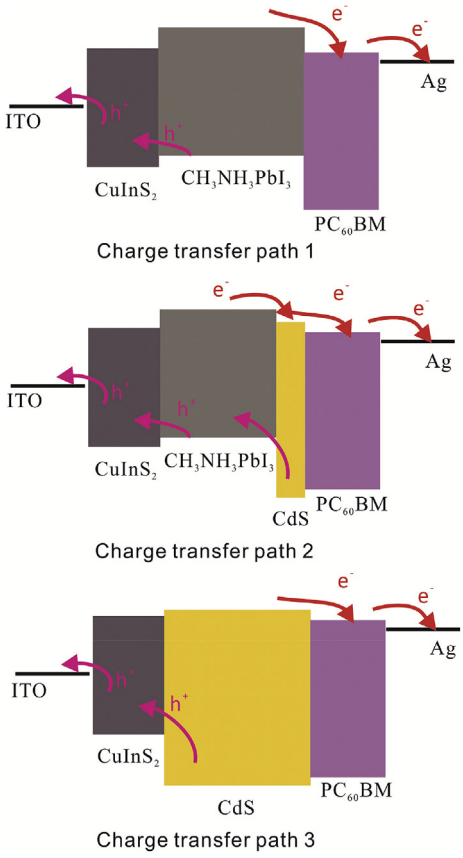

Fig. 7. Charge transfer paths for the ITO/$CuInS_2$/Al_2O_3/$CH_3NH_3PbI_3$:CdS/$PC_{60}BM$/Ag and ITO/$CuInS_2$/Al_2O_3/$CH_3NH_3PbI_3$:CdS/$PC_{60}BM$/Ag cells.

$PC_{60}BM$ interfaces leading to a decreased R_{CT2}. The EIS results indicate that the charge recombination in the ITO/$CuInS_2$/Al_2O_3/$CH_3NH_3PbI_3$:CdS/$PC_{60}BM$/Ag could be effectively reduced due to the introduction of CdS and would further improve the performance of the cell with CdS especially the J_{sc} and FF.

To prove that the CdS/$CuInS_2$ heterojunction can produce high current, the ITO/$CuInS_2$/CdS/$PC_{60}BM$/Ag cells are also fabricated and the characteristics of the cell under simulated AM 1.5 illumination (100 mW cm^{-2}) and dark conditions are shown in Fig. 5. The solar cell parameters of the ITO/$CuInS_2$/CdS/Ag cell shown in Table 1 are very close to the previously reported values [18]. Furthermore, the ITO/$CuInS_2$/CdS/Ag cell shows high photocurrent. In particular, the highest J_{sc} of the ITO/$CuInS_2$/CdS/$PC_{60}BM$/Ag cell reached (12.1 ± 0.3) mA cm^{-2}. These results confirm that the formed CdS/$CuInS_2$ heterojunction may make an important contribute to the enhancement of J_{sc} of the ITO/$CuInS_2$/Al_2O_3/$CH_3NH_3PbI_3$:CdS/$PC_{60}BM$/Ag cell.

Fig. 8 shows the IPCE spectra of the ITO/$CuInS_2$/Al_2O_3/$CH_3NH_3PbI_3$:CdS/$PC_{60}BM$/Ag and ITO/$CuInS_2$/Al_2O_3/$CH_3NH_3PbI_3$/$PC_{60}BM$/Ag cells, which displays a spectral response in the almost entire wavelength region from 300 to 850 nm for both types of solar cells. The trough in the IPCE spectra at around 400 nm should

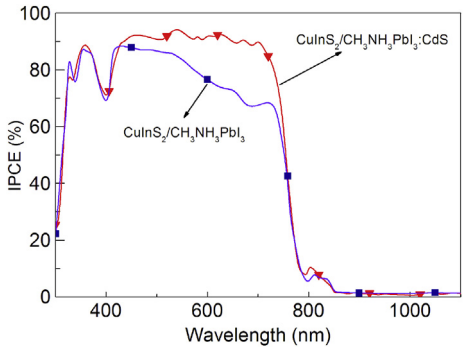

Fig. 8. IPCE spectra of the ITO/$CuInS_2$/Al_2O_3/$CH_3NH_3PbI_3$/$PC_{60}BM$/Ag and ITO/$CuInS_2$/Al_2O_3/$CH_3NH_3PbI_3$:CdS/$PC_{60}BM$/Ag cells.

be caused by the stronger refection of the glass/ITO substrates. For the ITO/$CuInS_2$/Al_2O_3/$CH_3NH_3PbI_3$:CdS/$PC_{60}BM$/Ag cell, an average IPCE of over 80% in the range of 300–800 nm can be observed. Furthermore, an IPCE peak at about 530 nm was observed, which is due to the decreased light absorption of CdS. For the ITO/$CuInS_2$/Al_2O_3/$CH_3NH_3PbI_3$/$PC_{60}BM$/Ag cell without CdS, the IPCE value is lower than that of the ITO/$CuInS_2$/Al_2O_3/$CH_3NH_3PbI_3$:CdS/$PC_{60}BM$/Ag cell in the wavelength region of 420–800 nm, which is consistent with the observed the UV–vis absorption spectra (Fig. 5a). The calculated J_{sc} value determined by integration of the IPCE values is 21.2 mA cm^{-2} (shown in Fig. S6), which is closed to the measured J_{sc} of (23.8 ± 0.2) mA cm^{-2}. There may be several factors for this discrepancy between the calculated J_{sc} and measured J_{sc}. The first factor may be that there is a different spectral response between the reference silicon solar cell and the measured perovskite solar cells. The second factor may be that the active area of the cell is not exactly equal to that of light spot (monochromatic illumination) during the IPCE measurements. If the effective area of the cell is larger than that of light spot, the non-illuminated part of the cell as a shunting load will be in parallel with the input resistance of IPCE current amplifier and therefore leads to a decreased IPCE. However, for *J*-V measurement, the shunt resistance of the non-illuminated part is still small compared to the total shunt resistance of the cell and therefore has little effect on measured J_{sc}, which leads to the discrepancy between the calculated J_{sc} and measured J_{sc}. To display the reproducibility of performance, more than 30 ITO/$CuInS_2$/Al_2O_3/$CH_3NH_3PbI_3$:CdS/$PC_{60}BM$/Ag cells were repeated. The corresponding statistics of the PCE are shown in Fig. S7.

4. Conclusions

In summary, perovskite solar cells based on $CH_3NH_3PbI_3$:CdS film with the $CuInS_2$ as a hole transporting layer are successfully fabricated by a precursor blending solution method for the first time. Our experimental results demonstrate that the introduced CdS in the $CH_3NH_3PbI_3$:CdS active layer increases the light absorption and the formed $CH_3NH_3PbI_3$/CdS bulk heterojunction reduces the charge recombination, which leads to a high photocurrent of the ITO/$CuInS_2$/Al_2O_3/$CH_3NH_3PbI_3$:CdS/$PC_{60}BM$/Ag cell. The highest J_{sc} measured for the ITO/$CuInS_2$/Al_2O_3/

$CH_3NH_3PbI_3$:CdS/$PC_{60}BM$/Ag cell is (23.8 ± 0.2) mA cm^{-2} and the calculated J_{sc} value determined by integration of the IPCE values is 21.20 mA cm^{-2}. Furthermore, the formed CdS/$CuInS_2$ heterojunction also contributes to the enhanced photocurrent. The power conversion efficiency of (16.5 ± 0.2)% is achieved with the best device, i.e., ca. 59% higher than that of the ITO/$CuInS_2$/Al_2O_3/$CH_3NH_3PbI_3$:CdS/$PC_{60}BM$/Ag cell without CdS. Actually, the method used in present study is expected to fabricate perovskite solar cells based on other types of perovskite/sulfide bulk heterojunctions. Therefore, our findings open new routes for the design and fabrication of high-efficient and solution processed bulk heterojunction solar cells.

Acknowledgment

This work was mainly supported by the Henan University Distinguished Professor Startup Fund, National Natural Science Foundation of China-Talent Training Fund of Henan (U1404616), National Natural Science Foundation of China (11274307, 91333121 and 11474286), Seed Fund of Young Scientific Research Talents of Henan University (CX0000A40540), International Cooperation Project of Henan Province (162102410083), and Research Fund of Henan University (2013YBZR046).

Appendix A. Supplementary data

Supplementary data related to this article can be found at http://dx.doi.org/10.1016/j.jpowsour.2016.12.027.

References

[1] A. Kojima, K. Teshima, Y. Shirai, T. Miyasaka, Organometal halide perovskites as visible-light sensitizers for photovoltaic cells, J. Am. Chem. Soc. 131 (2009) 6050–6051.
[2] H. Zhou, Q. Chen, G. Li, S. Luo, T.-b. Song, H.-S. Duan, Z. Hong, J. You, Y. Liu, Y. Yang, Interface engineering of highly efficient perovskite solar cells, Science 345 (2014) 542–546.
[3] W.S. Yang, J.H. Noh, N.J. Jeon, Y.C. Kim, S. Ryu, J. Seo, S.I. Seok, High-performance photovoltaic perovskite layers fabricated through intramolecular exchange, Science 348 (2015) 1234–1237.
[4] Q. Dong, Y. Fang, Y. Shao, P. Mulligan, J. Qiu, L. Cao, J. Huang, Electron-hole diffusion lengths> 175 μm in solution-grown $CH_3NH_3PbI_3$ single crystals, Science 347 (2015) 967–970.
[5] M.M. Lee, J. Teuscher, T. Miyasaka, T.N. Murakami, H.J. Snaith, Efficient hybrid solar cells based on meso-superstructured organometal halide perovskites, Science 338 (2012) 643–647.
[6] N.G. Park, Organometal perovskite light absorbers toward a 20% efficiency low-cost solid-state msoscopic solar cell, J. Phys. Chem. Lett. 4 (2013) 2423–2429.
[7] G.C. Xing, N. Mathews, S.Y. Sun, S.S. Lim, Y.M. Lam, M. Grätzel, S. Mhaisalkar, T.C. Sum, Long-range balanced electron- and hole-transport lengths in organic-inorganic $CH_3NH_3PbI_3$, Science 342 (2013) 344–347.
[8] M.Z. Liu, M.B. Johnston, H.J. Snaith, Efficient planar heterojunction perovskite solar cells by vapour deposition, Nature 501 (2013) 395–398.
[9] J. Burschka, N. Pellet, S.J. Moon, R. Humphry-Baker, P. Gao, M.K. Nazeeruddin, M. Grätzel, Sequential deposition as a route to high-performance perovskite-sensitized solar cells, Nature 499 (2013) 316–319.
[10] Y.Z. Wu, A. Islam, X.D. Yang, C.J. Qin, J. Liu, K. Zhang, W.Q. Peng, L.Y. Han, Retarding the crystallization of PbI2 for highly reproducible planar-structured perovskite solar cells via sequential deposition, Energ Environ. Sci. 7 (2014) 2934–2938.
[11] P.W. Liang, C.Y. Liao, C.C. Chueh, F. Zuo, S.T. Williams, X.K. Xin, J.J. Lin, A.K.Y. Jen, Additive enhanced crystallization of solution-processed perovskite for highly efficient planar-heterojunction solar cells, Adv. Mater 26 (2014) 3748–3754.
[12] X. Song, W.W. Wang, P. Sun, W.L. Ma, Z.K. Chen, Additive to regulate the perovskite crystal film growth in planar heterojunction solar cells, Appl. Phys. Lett. 106 (033901) (2015).
[13] Y.J. Jeon, S. Lee, R. Kang, J.E. Kim, J.S. Yeo, S.H. Lee, S.S. Kim, J.M. Yun, D.Y. Kim, Planar heterojunction perovskite solar cells with superior reproducibility, Sci. Rep. 4 (2014) 6953.
[14] N.J. Jeon, J.H. Noh, Y.C. Kim, W.S. Yang, S. Ryu, S. Il Seol, Solvent engineering for high-performance inorganic-organic hybrid perovskite solar cells, Nat. Mater 13 (2014) 897–903.
[15] I. Hwang, M. Baek, K. Yong, Core/shell structured TiO_2/CdS electrode to enhance the light stability of perovskite solar cells, ACS Appl. Mater Interfaces 7 (2015) 27863–27870.
[16] I. Hwang, K. Yong, Novel CdS hole-blocking layer for photostable perovskite solar cells, ACS Appl. Mater Interfaces 8 (2016) 4226–4232.
[17] Y. Xu, M.A.A. Schoonen, The absolute energy positions of conduction and valence bands of selected semiconducting minerals, Am. Mineral. 85 (2000) 543–556.
[18] L. Li, N. Coates, D. Moses, Solution-processed inorganic solar cell based on in situ synthesis and film deposition of $CuInS_2$ nanocrystals, J. Am. Chem. Soc. 132 (2010) 22–23.
[19] Y. Fu, F. Meng, M.B. Rowley, B.J. Thompson, M.J. Shearer, D. Ma, R.J. Hamers, J.C. Wright, S. Jin, Solution growth of single crystal methylammonium lead halide perovskite nanostructures for optoelectronic and photovoltaic applications, J. Am. Chem. Soc. 137 (2015) 5810–5818.
[20] J.H. Im, I.H. Jang, N. Pellet, M. Grätzel, N.G. Park, Growth of $CH_3NH_3PbI_3$ cuboids with controlled size for high-efficiency perovskite solar cells, Nat. Nanotechnol. 9 (2014) 927–932.
[21] S. Yang, Y.C. Zheng, Y. Hou, X. Chen, Y. Chen, Y. Wang, H.J. Zhao, H.G. Yang, Formation Mechanism of freestanding $CH_3NH_3PbI_3$ functional crystals: in situ transformation vs dissolution-crystallization, Chem. Mater 26 (2014) 6705–6710.
[22] T. Baikie, Y.N. Fang, J.M. Kadro, M. Schreyer, F.X. Wei, S.G. Mhaisalkar, M. Graetzel, T.J. White, Synthesis and crystal chemistry of the hybrid perovskite (CH_3NH_3) PbI_3 for solid-state sensitised solar cell applications, J. Mater Chem. A 1 (2013) 5628–5641.
[23] Z. Xiao, C. Bi, Y. Shao, Q. Dong, Q. Wang, Y. Yuan, C. Wang, Y. Gao, J. Huang, Efficient, high yield perovskite photovoltaic devices grown by interdiffusion of solution-processed precursor stacking layers, Energ Environ. Sci. 7 (2014) 2619–2623.
[24] C. Chen, Y. Xie, G. Ali, S.H. Yoo, S.O. Cho, Improved conversion efficiency of CdS quantum dots-sensitized TiO_2 nanotube array using ZnO energy barrier layer, Nanotechnology 22 (015202) (2011).
[25] A.R. Pascoe, N.W. Duffy, A.D. Scully, F. Huang, Y.B. Cheng, Insights into planar $CH_3NH_3PbI_3$ perovskite solar cells using impedence spectroscopy, J. Phys. Chem. C 119 (2015) 4444–4453.
[26] H. Kim, J. Lee, N. Yantara, P. Boix, S. Kulkarni, S. Mhaisalkar, M. Grätzel, N. Park, High efficiency solid-state sensitized solar cell-based on submicrometer rutile TiO_2 nanorod and $CH_3NH_3PbI_3$ perovskite sensitizer, Nano Lett. 13 (2013) 2412–2417.
[27] G. Niu, W. Li, F. Meng, L. Wang, H. Dong, Y. Qiu, Study on the stability of $CH_3NH_3PbI_3$ films and the effect of post-modification by aluminum oxide in all-solid-state hybrid solar cells, J. Mater. Chem. A 2 (2014) 705–710.